Evidence of linear relationships between clear-sky indices in photosynthetically active radiation and broadband ranges

William Wandji Nyamsi, Yves-Marie Saint-Drenan, John A. Augustine, Antti Arola, Lucien Wald

Meteorol. Z. (Contrib. Atm. Sci.), Vol. 33, No. 2, 117–129 (published online March 27, 2024)

Evidence of linear relationships between clear-sky indices in photosynthetically active radiation and broadband ranges

William Wandji Nyamsi[1,2,5*], Yves-Marie Saint-Drenan[3], John A. Augustine[4], Antti Arola[2] and Lucien Wald[3]

[1]Finnish Meteorological Institute, Helsinki, Finland.
[2]Finnish Meteorological Institute, Kuopio, Finland
[3]MINES PSL, Centre 0.I.E., Sophia Antipolis, France
[4]NOAA Global Monitoring Laboratory, Boulder, CO, USA
[5]Department of Physics, Faculty of Science, University of Yaoundé 1, Cameroon

(Manuscript received July 1, 2023; accepted October 4, 2023)

Abstract

This study provides empirical relationships between photosynthetically active radiation (PAR) and broadband clear-sky indices at ground level for both the PAR global irradiance and its direct component. Once multiplied by the irradiance in clear-sky conditions, the clear-sky index provides the irradiance under cloudy conditions. The relationships are developed by the means of radiative transfer simulations of various realistic atmospheric states including both ice and water cloud phases. For the direct component, the PAR clear-sky index is equal to the broadband clear-sky index. For global irradiance, several linear relationships are proposed depending on the availability of cloud properties namely cloud phase and cloud optical depth. The developed relationships are validated numerically and experimentally by using ground-based measurements from the SURFRAD network in the U.S.A. Overall, it has been found, a squared correlation coefficient R^2 close to 1.00 and a relative bias (relative root mean square error) in absolute value less than 3 % (6 %) with respect to the means of the relevant measurements, demonstrating a high level of accuracy of the proposed relationships.

Keywords: Broadband irradiance, clear-sky, clear-sky index, cloud, photosynthetically active radiation, radiative transfer simulations

1 Introduction

Solar irradiance reaching the Earth's surface within the spectral range from 0.40 µm to 0.70 µm is called photosynthetically active radiation (PAR). It is one of the most important sources of energy for the development of biomass where it is exploited by leaves of plants or plankton in the waters through the photosynthesis process (McCree, 1981; Frolking et al., 1998; Frouin and Murakami, 2007). PAR is defined as the power per unit area coming from the sun in the form of electromagnetic radiation reaching the ground level on a horizontal plane and integrated over the PAR spectral range thus expressed in $\mathrm{W\,m^{-2}}$. Another well-known term dedicated to PAR is photosynthetic photon flux density (PPFD). The latter is defined as the total quantity of photons received in the same spectral range per unit area per unit time, thus expressed in $\mathrm{\mu mol\,m^{-2}\,s^{-1}}$. Both PAR and PPFD are connected by the widely used approximation of McCree (1972): $1\,\mathrm{W\,m^{-2}} \approx 4.57\,\mathrm{\mu mol\,m^{-2}\,s^{-1}}$.

Farmers, growers, meteorologists, practicians and scientists in agriculture, forestry and oceanography are in growing need of high–quality PAR data but also its direct component that comes from the direction of the sun and its diffuse component that comes from the rest of the sky vault. Both components affect plants in different manner, e.g., the diffuse component produces a more homogeneous light profile in the canopy than the direct component (Li and Yang, 2015).

High-quality PAR measurements can be obtained by the means of reference instruments, quantum sensors for instance (Light Measurement. Available online: https://www.licor.com/documents/3bjwy50xsb49jqof0wz4, accessed on 2023-03-01). Nevertheless, such measurements still lack spatial and temporal coverage yielding researchers to estimate PAR from measurements or estimates of the broadband irradiance, i.e., irradiance integrated over the broadband range from 0.28 µm to approximately 3 µm. Such measurements or estimates are significantly more frequently available in space and time and originate from ground-based instruments or are derived from satellite images or meteorological analyses (Udo and Aro, 1999; Zhang et al., 2000; Mottus et al., 2001; Gonzalez and Calbo, 2002, Jacovides et al., 2004, 2015, Escobedo et al., 2009; Akitsu et al., 2015; Vindel et al., 2018; Thomas et al., 2019). The above approaches assume a proportionality coefficient between broadband and PAR irradiances which is empirically determined from coincident data sets of measurements of both broadband radiation and PAR. However, the accu-

*Corresponding author: William Wandji Nyamsi, Department of Physics, Faculty of Science, University of Yaoundé 1, P.O. Box 812 Yaoundé, Cameroon, e-mail: william.wandji@fmi.fi

DOI 10.1127/metz/2023/1203

Gebrüder Borntraeger Science Publishers, Stuttgart, www.borntraeger-cramer.com

racy of such relationships is not guaranteed outside the climates and periods of time for which they were developed.

To overcome this problem and aiming at more universal relationships, several approaches rely on estimating PAR fluxes as the product of the clear-sky PAR fluxes (Bosch et al., 2009; Wandji Nyamsi et al., 2014; 2015a) by a physical quantity accounting for the attenuation due only to clouds often called clear-sky index or also called cloud modification factor (Oumbe et al., 2014). The latter close to 1 would indicate an atmosphere under clear-sky conditions, whereas when close to 0 would probably indicate an atmosphere totally covered by thick clouds, and when above 1 would mean enhancement effects that may occur over short periods of time in broken-clouds conditions (Calbo et al., 2005; Sabburg and Calbo, 2009; Piedehierro et al., 2014).

The modelling of the clear-sky index has been widely reported in the literature for broadband and UV ranges (Krotkov et al., 2001; Calbo et al., 2005; Den Outer et al., 2010; Huang et al., 2011; Oumbe et al., 2014). Unfortunately, similar investigations were not yet carried out for the PAR range. Therefore, the objective of this article is to extend the clear-sky index to the PAR range of the solar spectrum by investigating and developing the relationship between the PAR clear-sky index noted K_c^{PAR} and the broadband clear-sky index noted K_c^{BB} under various realistic sky conditions. This new study on the link between K_c^{PAR} and K_c^{BB} leverages on recent results and advances on the availability of K_c^{BB} from widely used satellite–based algorithms such as HelioClim-3 version 5 (HC3v5), Climate Monitoring Satellite Application Facility (CM-SAF) and Copernicus Atmosphere Monitoring Service Radiation Service (CAMS-Rad) products (Gschwind et al., 2006; Mueller et al., 2012; Qu et al., 2017). The present study aims at fulfilling three main constraints: (1) the algorithm can be implemented for routine operation, (2) it should be simple and (3) the outcomes of the algorithm should be accurate at any location any time. From our extensive review of the literature, it is the first time that a study on the relationship between K_c^{PAR} and K_c^{BB} is carried out in a detailed manner.

The paper is structured as follows. In Section 2, a problem statement is formally described aiming at expressing K_c^{PAR} as a function of K_c^{BB}. The methodology is presented in Section 3 that calls upon radiative transfer simulations (RTS) and ground–based measurements. Then, inputs to the radiative transfer model and ground–based measurements are described in Section 4. The resulting relationships are discussed and validated in Section 5. How to use these relationships is presented in Section 6. Section 7 concludes the study.

2 Problem statement

Let λ be the wavelength in nm, G_λ and B_λ the spectral global irradiance and its direct component, respectively, under all-sky conditions and $G_{\lambda\_\mathrm{clear}}$ and $B_{\lambda\_\mathrm{clear}}$ the corresponding quantities under clear-sky conditions. If the superscript BB denotes the broadband range of [0.28, 3] µm, the broadband global irradiance G^{BB} and its direct component B^{BB} are given by:

$$G^{\mathrm{BB}} = \int_{280}^{3000} G_\lambda d\lambda \tag{2.1}$$

$$B^{\mathrm{BB}} = \int_{280}^{3000} B_\lambda d\lambda \tag{2.2}$$

The clear-sky global irradiance $G_{\mathrm{clear}}^{\mathrm{BB}}$ and its direct component $B_{\mathrm{clear}}^{\mathrm{BB}}$ are given by:

$$G_{\mathrm{clear}}^{\mathrm{BB}} = \int_{280}^{3000} G_{\lambda\_\mathrm{clear}} d\lambda \tag{2.3}$$

$$B_{\mathrm{clear}}^{\mathrm{BB}} = \int_{280}^{3000} B_{\lambda\_\mathrm{clear}} d\lambda \tag{2.4}$$

Similarly, the PAR global irradiance G^{PAR} and its direct component B^{PAR}, and the corresponding quantities but for clear-sky conditions $G_{\mathrm{clear}}^{\mathrm{PAR}}$ and $B_{\mathrm{clear}}^{\mathrm{PAR}}$ are given by:

$$G^{\mathrm{PAR}} = \int_{400}^{700} G_\lambda d\lambda \tag{2.5}$$

$$B^{\mathrm{PAR}} = \int_{400}^{700} B_\lambda d\lambda \tag{2.6}$$

$$G_{\mathrm{clear}}^{\mathrm{PAR}} = \int_{400}^{700} G_{\lambda\_\mathrm{clear}} d\lambda \tag{2.7}$$

$$B_{\mathrm{clear}}^{\mathrm{PAR}} = \int_{400}^{700} B_{\lambda\_\mathrm{clear}} d\lambda \tag{2.8}$$

Then, the global and direct broadband clear-sky indices K_c^{BB} and K_{cB}^{BB} are defined as:

$$K_c^{\mathrm{BB}} = G^{\mathrm{BB}} / G_{\mathrm{clear}}^{\mathrm{BB}} \tag{2.9}$$

$$K_{cB}^{\mathrm{BB}} = B^{\mathrm{BB}} / B_{\mathrm{clear}}^{\mathrm{BB}} \tag{2.10}$$

Similar definitions hold for the global and direct PAR clear-sky indices K_c^{PAR} and K_{cB}^{PAR}:

$$K_c^{\mathrm{PAR}} = G^{\mathrm{PAR}} / G_{\mathrm{clear}}^{\mathrm{PAR}} \tag{2.11}$$

$$K_{cB}^{\mathrm{PAR}} = B^{\mathrm{PAR}} / B_{\mathrm{clear}}^{\mathrm{PAR}} \tag{2.12}$$

The objective is thus to develop simple, accurate, fast and easy-to-implement relationships as follows: $K_c^{\mathrm{PAR}} = f\left(K_c^{\mathrm{BB}}\right)$ and $K_{cB}^{\mathrm{PAR}} = f\left(K_{cB}^{\mathrm{BB}}\right)$.

Once K_c^{PAR} is known, PAR for all-sky conditions G^{PAR} is obtained by multiplying K_c^{PAR} by the outcome of an appropriate model providing the PAR in clear-sky conditions $G_{\mathrm{clear}}^{\mathrm{PAR}}$. Similarly, the direct component B^{PAR} is obtained by multiplying K_{cB}^{PAR} by the direct component of the PAR in clear-sky conditions $B_{\mathrm{clear}}^{\mathrm{PAR}}$. The diffuse component D^{PAR} is then given by G^{PAR} minus B^{PAR}.

3 Methodology

Overall, the study calls upon a radiative transfer model (RTM) that simulates the propagation of solar radiation in various sky conditions, including clear-sky conditions, for both the PAR and broadband spectral ranges. A large number of quadruplets (G^{PAR}, $G^{\mathrm{PAR}}_{\mathrm{clear}}$, G^{BB}, $G^{\mathrm{BB}}_{\mathrm{clear}}$) and ($B^{\mathrm{PAR}}$, $B^{\mathrm{PAR}}_{\mathrm{clear}}$, B^{BB}, $B^{\mathrm{BB}}_{\mathrm{clear}}$) are obtained from which the clear-sky indices (K_c^{PAR}, K_c^{BB}) and (K_{cB}^{PAR}, K_{cB}^{BB}) are computed. Several graphs between K_c^{PAR} and K_c^{BB} as well as between K_{cB}^{PAR} and K_{cB}^{BB} were made as functions of atmospheric variables. The shape of the curve would indicate the nature of the relationship and thus help to establish the relevant relationships. In order to take into account, the multiple cases faced by researchers and practitioners, we have established three groups of relationships. The first group deals with cases when both cloud optical depth (COD) and cloud phase are available. The second group deals with cases when cloud phase is available, but uncertainty on COD is too large making COD useless, while the third case deals with cases when no data on cloud properties is available.

Once the relationships are established, their outcomes are numerically validated by comparing them against results from detailed spectral calculations with the RTM and then validated against ground-based measurements of both PAR and broadband irradiances obtained from the surface radiation network described later serving as reference. The differences between estimates and reference values are computed and synthesized by the bias (mean error), standard deviation (STD) of errors, and root mean square error (RMSE) with their corresponding values rbias, rSTD and rRMSE relative to the mean value of the reference data following the ISO standard (1995). In addition, the squared correlation coefficient (coefficient of determination) R^2 is computed.

4 Radiative transfer simulations and ground-based measurements

4.1 Radiative transfer simulations

The RTM simulates the propagation of solar radiation through a cloudy atmosphere for various wavelengths. A large number of atmospheric states was randomly built by a Monte-Carlo technique and then each atmospheric state was input to the RTM. An atmospheric state in clear-sky conditions is a combination of the solar zenith angle θ_s, ground albedo ρ_g, total column contents in ozone and water vapor, vertical profile of temperature, pressure, density, and volume mixing ratio for gases as a function of altitude, aerosol optical depth at 550 nm, and aerosol type, and the elevation of the ground above sea level. In all-sky conditions, cloud properties, namely phase, effective radius of water droplets and ice crystals, COD at 550 nm noted τ_{cloud}, cloud base height and thickness, are added to the variables of the clear-sky atmospheric state.

Table 1 reports the range of values taken respectively by θ_s, ρ_g, and the seven other variables describing the clear-sky atmosphere. The random selection of inputs in this Table follows the modelled marginal distribution established from observations proposed by Lefèvre et al. (2013) and Oumbe et al. (2014) and used by e.g., Wandj Nyamsi et al., (2015b, 2017, 2021) or Gschwind et al. (2019). Specifically, the uniform distribution was chosen as a model for the marginal probability of all parameters except aerosol optical thickness and total column ozone. The chi-square law and the beta law were used for aerosol optical thickness and ozone, respectively. The selection of these parametric probability density functions and their corresponding parameters have been empirically determined from the analyses of the observations made in the AERONET network for aerosol properties and from meteorological satellite-based ozone products.

One hundred pairs of θ_s and ρ_g was associated with each of the 100 random selections of the other seven variables in Table 1 providing a set of 10 000 clear-sky atmospheric states. Then, each clear-sky atmospheric state was associated with one combination of τ_{cloud}, cloud base height, cloud geometrical thickness and cloud phase as reported in Table 2. Values are related to types of clouds to produce realistic conditions. This yielded 1 400 000 (10 000 clear-sky atmospheric states times 140 combinations of cloudy properties) atmospheric conditions for water clouds and 630 000 (10 000 clear-sky atmospheric states times 63 combinations of cloudy properties) atmospheric conditions for ice clouds.

This study was performed with the RTM libRadtran 2.0.4 (Mayer and Kylling, 2005; Emde et al., 2016). The pseudo-spectral calculation from LOWTRAN included in libRadtran was selected for the band parametrization of absorption cross sections. For all RTS, a 1D plane-parallel atmosphere was assumed and the DISORT 2.0 (discrete ordinate technique) algorithm (Stamnes et al., 1988, Stamnes et al., 2000) with 16 streams was selected to solve the radiative transfer equation because several articles have demonstrated the accuracy of its results when compared to robust and more time–consuming solvers. OPAC library of Hess et al. (1998) was selected for different aerosol models as listed in Table 1.

Default values of libRadtran were used for the cloud liquid water content and the droplet effective radius: 1.0 g m^{-3} and 10 µm for water clouds, and 0.005 g m^{-3} and 20 µm for ice clouds. In order to convert the microphysical properties of clouds i.e., cloud liquid content and droplet effective radius into their optical properties, the parameterization of Fu (1996) and Hu and Stamnes (1993) were used for ice and water clouds respectively. Other wavelengths were scaled accordingly. Single layer clouds were assumed in the computations in line with most operational radiative transfer retrieval algorithms. All other variables have been set to the default values of the RTM.

Table 1: Ranges and statistical distributions of values taken by the solar zenithal angle, the ground albedo, the elevation of the ground above mean sea level and the seven variables describing the clear-sky atmosphere.

Variable	**Value**
Solar zenithal angle (θ_s)	0.01, 10, 20, 30, 40, 50, 60, 70, 80, 89 (degree)
Ground spectral albedo ρ_g	0, 0.1, 0.2, 0.3, 0.4, 0.5, 0.6, 0.7, 0.8, 0.9
Elevation of the ground above mean sea level	Equiprobable in the set: 0, 1, 2, 3 in km
Total column content of ozone	Ozone content is $300\beta + 200$, in Dobson unit where β follows a Beta law, with parameters $A = 2$, and $B = 2$
Total column content in water vapor	Equiprobable between 0 and 70 kg m^{-2}
Atmospheric profiles (Air Force Geophysics Laboratory standards)	Equiprobable in the set: mid-latitude summer, mid-latitude winter, sub-Arctic summer, sub-Arctic winter, tropical US. standard atmosphere
Aerosol optical depth at 550 nm	Gamma distribution, with shape parameter = 2, and scale parameter = 0.13, mean = 0.25
Angstrom exponent coefficient	Normal distribution, with mean = 1.3 and standard deviation = 0.5
Aerosol mixture	Equiprobable in the set of the nine aerosol mixtures proposed in libRadtran: urban, continental average, continental clean, continental polluted, maritime clean, maritime polluted, maritime tropical, desert, Antarctic

Table 2: Selected cloud properties. Mostly from Oumbe et al. (2014). Types of clouds and their acronyms; cumulus (Cu); stratocumulus (Sc); altostratus (As); altocumulus (Ac); cirrus (Ci) and cirrostratus (Cs).

Cloud optical depth τ_{cloud}	Water clouds (cloud base height + thickness, km)	Ice clouds (cloud base height + thickness, km)
0.5, 1, 2, 3 (and 4 for ice cloud only)	Cu: 0.4+0.2, 1+1.6, 1.2+0.2, 2+0.5 Ac: 2+3, 3.5+1.5, 4.5+1	Ci: 6+0.5, 8+0.3, 10+1
5, 7, 10, 15, 20, 25, 30, 35 (and 40, 45, 50, 60, 70, 75, 80, 100 for ice cloud only)	Sc: 0.5+0.5, 1.5+0.6, 2+1, 2.5+2 As: 2+3, 3.5+2, 4.5+1	Cs: 6+0.5, 8+2, 10+1
40, 45, 50, 70, 75, 80, 90, 100	St: 0.2+0.5, 0.5+0.3, 1+0.5 Ns: 0.8+3, 1+1 Cb: 1+6, 2+8	–

For all RTS, the solar spectrum of Gueymard (2004) was used because it was the most spectrally detailed available in libRadtran at that time. Its spectral resolution is 0.5 nm in the range [0.28, 0.4] µm, 1 nm in [0.4, 1.700] µm and 5 nm in [1.705, 4] µm. The wavelength range was set between 0.28 and 3 µm yielding spectral irradiances from detailed spectral calculations i.e., nm per nm. libRadtran was run twice: one in order to produce the spectral irradiances in clear-sky conditions G_{λ_clear} and B_{λ_clear}, the second in order to produce the spectral irradiances in cloudy conditions G_λ and B_λ and ($G^{\text{PAR}}_{\text{RTS}}$, $G^{\text{PAR}}_{\text{clear\_RTS}}$, $B^{\text{PAR}}_{\text{RTS}}$, $B^{\text{PAR}}_{\text{clear\_RTS}}$) following Eqs. (2.1)–(2.8), and then the simulated clear-sky indices ($K^{\text{BB}}_{\text{c\_RTS}}$, $K^{\text{BB}}_{\text{cB\_RTS}}$) and ($K^{\text{PAR}}_{\text{c\_RTS}}$, $K^{\text{PAR}}_{\text{cB\_RTS}}$) following Eqs. (2.9)–(2.12).

Our simulations consider clouds as infinite, homogenous and 1D parallel layers referring to overcast sky situations. In the reality, cloudy situations might also comprise broken cloudy situations. For instance, we analysed the series of ground-based measurements used for the validation and described later. This series include a quantity called fractional sky cover (FSC) that describes the state of the cloud cover. FSC greater than 0.95 means overcast sky situations. The lower FSC, the more broken the cloud cover. We selected the cloudy situations with appropriate flagged value, and we found that 42 % of data are under broken cloudy situations i.e., for FSC less than 0.95. This example shows how frequent broken cloud cover can be. Although the parametrizations used are originally in 3D cloud effects, unfortunately, the selected version of the RTM cannot appropriately handle atmospheres comprising broken clouds. This will require more sophisticated simulations and a large number of configurations of broken clouds should be designed. Regarding the striking level of complexity, this study does not take into account these cases.

4.2 Ground-based measurements

One-minute averages of high-quality measurements with acquisition frequency of 1 Hz were collected from the surface radiation (SURFRAD) network through the SURFRAD FTP Server (available online: https://gml.noaa.gov/aftp/data/radiation/surfrad/, accessed on 2022-10-01) at seven ground–based stations located in the U.S.A. The measurement period used spans over 5 years, from 2016-01-01 to 2020-12-31. Fig.1 shows

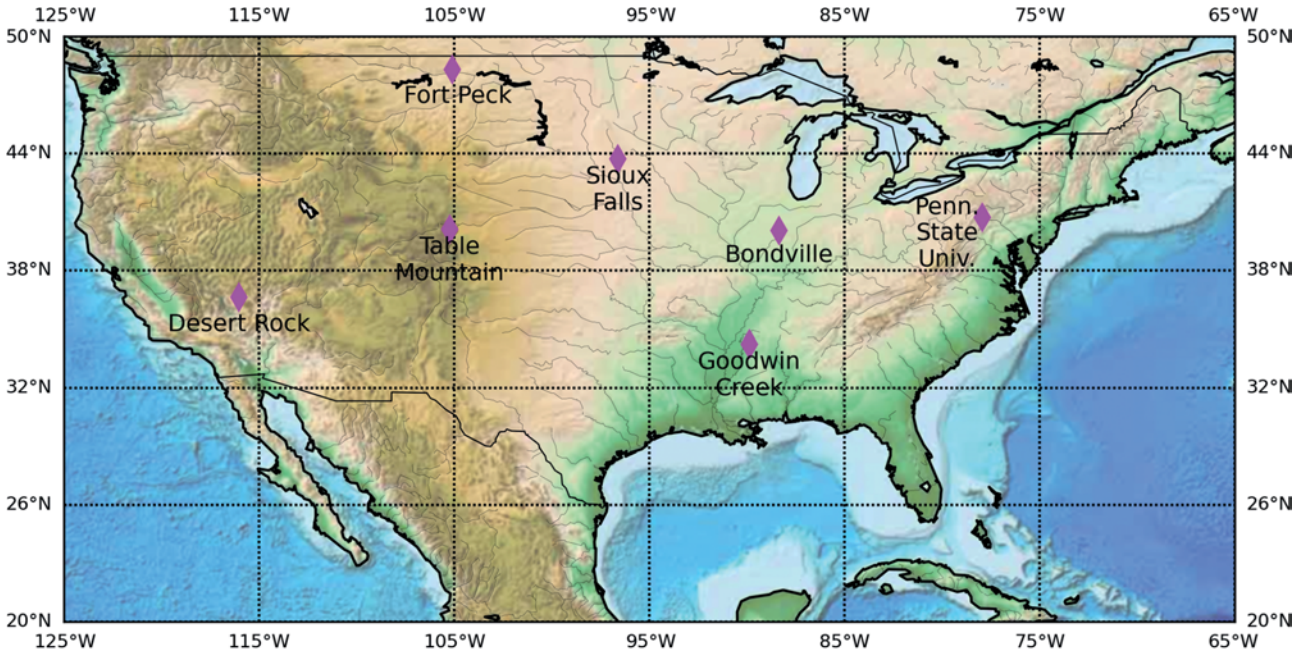

Figure 1: Map of the seven SURFRAD sites. The orographic basemap is under public domain and is from the Etopo1 data set from the National Oceanic and Atmospheric Administration of the United States of America.

Table 3: Ground-based stations used for measurement collection, from the northernmost station to the southernmost one.

Station	Fort Peck	Sioux Falls	Penn. State Univ	Table Mountain	Bondville	Desert Rock	Goodwin Creek
Code	FPK	SXF	PSU	TBL	BON	DRA	GWN
Latitude (°)	48.31	43.73	40.72	40.12	40.05	36.62	34.25
Longitude (°)	−105.10	−96.62	−77.93	−105.24	−88.37	−116.02	−89.87
Elevation amsl (m)	634	473	376	1689	230	1007	98

*amsl: above mean sea level.

the geographical distribution of the stations and Table 3 lists them with their respective three-letter station identifier, latitude, longitude, and elevation above the mean seal level. The reader may refer to Wandji Nyamsi et al. (2019) for a detailed description of climate and ground characteristics at each station. Collected measurements include broadband global irradiances and their diffuse and direct components and PAR global irradiances. No direct or diffuse components of the PAR irradiance are available. Table 4 reports the measuring instruments, their spectral range and uncertainty.

The SURFRAD collection includes a series of products named "*RadFlux*" generated following the Radiative Flux (RadFlux) Analysis methodology (Long and Ackerman, 2000). In brief, this methodology is based on a technique using measured broadband irradiances for selecting clear-sky periods. The clear-sky selection algorithm used is comparable to other published ones (Wandji Nyamsi et al., 2023). Then, functions are fitted on the detected clear-sky data and then exploited to produce continuous clear-sky estimates. The clear-sky estimates and measurements are then used in various ways to infer cloud optical properties (Barnard et al., 2008; Long, 2005; Long and Ackerman, 2000; Long and Gaustad, 2004; Long et al., 2006). Among these "*RadFlux*" products, the high–quality ones used here are clear-sky broadband global irradiance, FSC and COD. In addition, data were flagged (flag "ClrF") 1 and 0 if measured under clear-sky and cloudy sky conditions respectively, while cloud optical depth were flagged (flag "TauF") 1 and 0 if the cloud phase were water or ice respectively. Overall, only measurements of irradiance greater than 0 were used in this study.

Experimental validations of the developed relationships were carried out with appropriate SURFRAD data. For doing so, clear-sky PAR fluxes should be initially produced with high accuracy. Keeping only data with flag "ClrF" equal to 1 and assuming that the clear-sky periods identified by analyzing broadband irradiances are also clear-sky periods for PAR measurements, both measured PAR and broadband fluxes are selected corresponding to clear-sky conditions at each station. A conversion factor of $\alpha = 0.422 \pm 0.006$ is used to convert broadband fluxes to PAR with very high accuracy. Incidentally, this value 0.42 is approximately the ratio of the PAR to the broadband irradiances at the top of the atmosphere when using the solar spectrum of Gueymard (2004) (see e.g., Table 3.3 in Wald, 2021). This coefficient is then applied on the time series of "*RadFlux*" clear-sky broadband irradiance yielding time se-

Table 4: List of instruments used at each station.

Measurement	Instrument	Wavelength range	Estimated 95 % Uncertainty	Reference
Broadband diffuse component	Eppley 8-48 "black and white" pyranometer	280 to 3000 nm	3 % or 4 W m^{-2}	Table of uncertainties*
Broadband direct component	Kipp & Zonen, model CHP1	280 to 3000 nm	2 % or [5, 7] W m^{-2}	MICHALSKY et al., 2011
Broadband global irradiance	Spectrolab SR-75 pyranometer	280 to 3000 nm	6 % or 10 W m^{-2}	Table of uncertainties*
PAR global irradiance	LI-COR Quantum (PAR) Sensor	400 to 700 nm	Total error approximately between 5 % and 8 %	AUGUSTINE et al., 2000 Light Measurement**.

* Available online: https://gml.noaa.gov/aftp/data/radiation/surfrad/RadFlux/RadFlux_Uncert_Table.pdf, accessed on 2022-11-01
** Available online: https://www.licor.com/documents/3bjwy50xsb49jqof0wz4, accessed on 2023-03-01.

ries of "*RadFlux*" clear-sky PAR irradiance. Time series of measured $K_{\mathrm{c\_meas}}^{\mathrm{BB}}$ and $K_{\mathrm{c\_meas}}^{\mathrm{PAR}}$ are produced by dividing "*RadFlux*" broadband irradiances, respectively PAR irradiances, by "*RadFlux*" clear-sky broadband and PAR irradiances. Then, estimated $K_{\mathrm{c\_est}}^{\mathrm{PAR}}$ computed by the developed relationships using measured $K_{\mathrm{c\_meas}}^{\mathrm{BB}}$, "*RadFlux*" τ_{cloud} as well as cloud phase as inputs, are compared to measured $K_{\mathrm{c\_meas}}^{\mathrm{PAR}}$. If "*RadFlux*" τ_{cloud} is greater than 100, it is set to 100 for computational reasons. The flag "TauF" is used for selection as 1 for water clouds and 2 for ice clouds for discriminating cloud phase. All experimental comparisons deal only with overcast situations, i.e., data for which FSC is greater than 0.95.

5 Results and discussion

5.1 Direct clear-sky index

In the case of the direct clear-sky index, only the presence of clouds in the line of sight of the sun matters whether it is an overcast situation or a broken-cloud situation. Hence, both sky conditions can be handled with any RTM. Fig. 2 displays simulated direct broadband clear-sky indices ($K_{\mathrm{cB\_RTS}}^{\mathrm{BB}}$ on horizontal axis) against simulated PAR clear-sky indices ($K_{\mathrm{cB\_RTS}}^{\mathrm{PAR}}$ on vertical axis) for all atmospheric states: left side for ice clouds and right side for water clouds. Whatever the cloud phase, all points in the graph are very well distributed along the 1:1 line with little deviation. All the variability contained in $K_{\mathrm{cB\_RTS}}^{\mathrm{BB}}$ is entirely captured by $K_{\mathrm{cB\_RTS}}^{\mathrm{PAR}}$ despite that a very few points lie above the 1:1 line. Overall, the relationship between $K_{\mathrm{cB\_RTS}}^{\mathrm{PAR}}$ and $K_{\mathrm{cB\_RTS}}^{\mathrm{BB}}$ is clearly linear so that, for both cloud phases, one can state that $K_{cB}^{\mathrm{PAR}} = K_{cB}^{\mathrm{BB}}$ without losing noticeable accuracy. Hence, there is only one relationship which is simply the identity function.

Since no direct PAR measurements were available, we performed a kind of validation by using as reference another set of libRadtran simulations (K_{cB}^{BB}, K_{cB}^{PAR}) built randomly following the distribution of variables described in Tables 1 and 2. The accuracy of the proposed relationship is evidenced by comparing this new set of simulated K_{cB}^{PAR} to the new set of K_{cB}^{BB} since they are nearly identical. Table 5 reports the statistical indicators obtained for numerical validations and reveals a high level of accuracy of the proposed relationship since these statistical indicators are close to 0 and the squared correlation coefficient R^2 is equal to 1.00.

Table 5: Statistical indicators of the performances of the developed relationship for estimating K_{cB}^{PAR} as equal to K_{cB}^{BB} for numerical validations.

	Ice cloud	Water cloud
Number of data	630000	1400000
Mean	0.0333	0.0386
Bias (rbias)	−0.0001 (−0.1 %)	−0.0006 (−1.6 %)
STD (rSTD)	0.0001 (0.4 %)	0.00015 (3.9 %)
RMSE (rRMSE)	0.0001 (0.4 %)	0.0016 (4.2 %)
R^2	1.0000	1.0000

5.2 Clear-sky index

5.2.1 For cases when COD and cloud phase are available

Fig. 3 is an example of scatterplot between simulated global broadband ($K_{\mathrm{c\_RTS}}^{\mathrm{BB}}$ on horizontal axis) and PAR ($K_{\mathrm{c\_RTS}}^{\mathrm{PAR}}$ on vertical axis) clear-sky indices as a function of the solar zenithal angle, for $\tau_{\mathrm{cloud}} = 30$ and ice (3a) and water (3b) clouds separately. Overall, $K_{\mathrm{c\_RTS}}^{\mathrm{PAR}}$ is always greater than $K_{\mathrm{c\_RTS}}^{\mathrm{BB}}$ whatever the atmospheric state, indicating that the PAR radiation is less attenuated by clouds than the broadband radiation. In other words, the PAR radiation penetrates the cloud more effectively than the broadband radiation. For $\tau_{\mathrm{cloud}} \leq 5$, an enhancement effect of the radiation due to the presence of clouds is observed as well as evidence that the amplitude of this effect is larger on PAR than on broadband radiation (not shown). Such an effect has been reported in the literature for UV irradiances (CALBO et al., 2005; SABBURG and CALBO, 2009). In Fig. 3, the spread of coloured dots

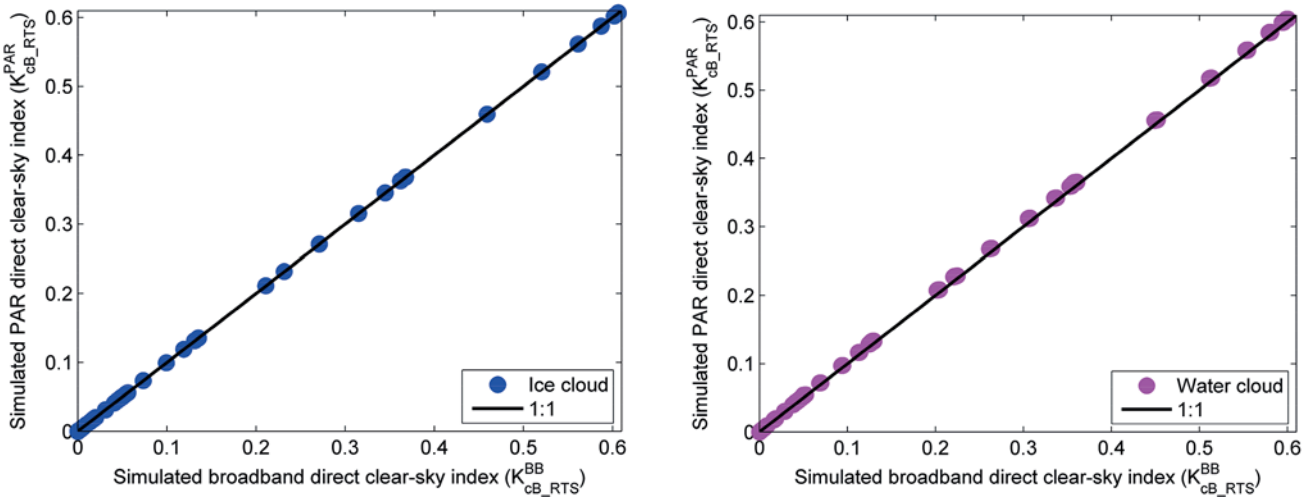

Figure 2: Scatterplot between broadband ($K^{BB}_{cB\_RTS}$ on horizontal axis) and PAR ($K^{PAR}_{cB\_RTS}$ on vertical axis) direct clear-sky indices for all atmospheric states. Left and right sides are for ice and water clouds respectively. 1:1 line is the perfect line.

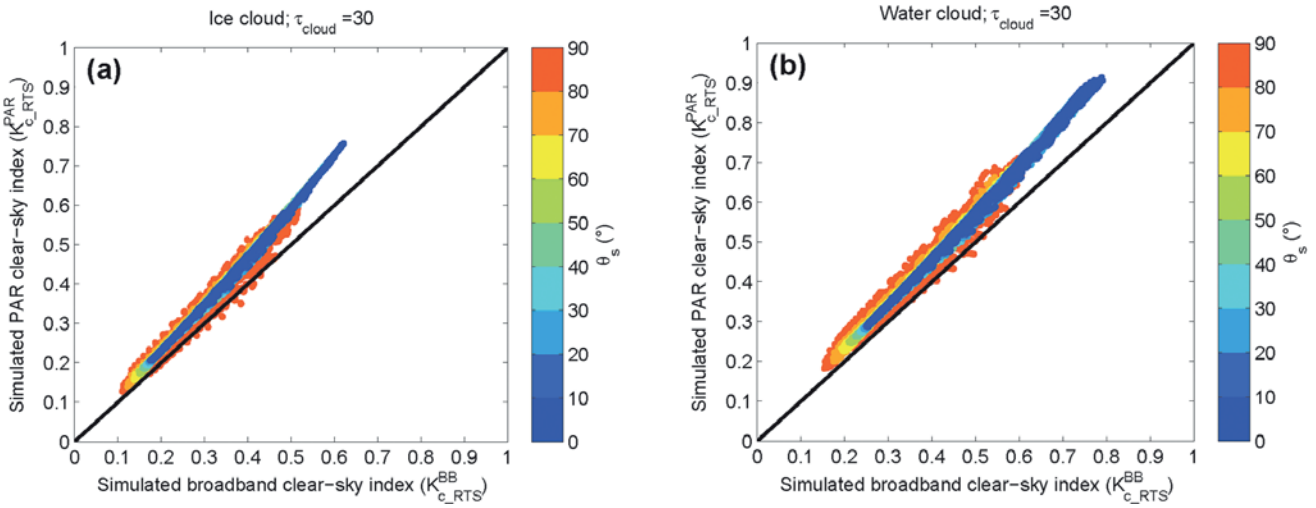

Figure 3: Scatterplot between broadband ($K^{BB}_{c_RTS}$on horizontal axis) and PAR ($K^{PAR}_{c\_RTS}$ on vertical axis) clear-sky indices for various classes of the solar zenithal angle θ_s for τ_{cloud} = 30. (a) for ice clouds and (b) for water clouds. The color bar indicates the θ_s range.

for each class of θ_s is very limited except for the class]80°, 90°]. The coloured dots are superimposed meaning that the difference between the broadband and PAR clear-sky indices is weakly dependent on θ_s. The difference between both clear-sky indices increases with increasing $K^{BB}_{c\_RTS}$. For both cloud phases, R^2 is equal to 1.00 with a very limited dispersion of points denoting that the variability contained in $K^{BB}_{c\_RTS}$ is entirely transferred into $K^{PAR}_{c\_RTS}$. This result clearly shows existence of a linear relationship between the clear-sky indices. The impact due to the wavelength–dependence of ground albedo has been investigated by replacing ρ_g in Table 1 by various spectral albedos covering four realistic categories of surface: vegetation, soil, manmade materials, and water taken from the large collection of spectral albedos available online: https://speclib.jpl.nasa.gov/library (accessed on 2022-11-01). The analysis reveals that the shape of the curve is not sensitive to the wavelength–dependence of the ground albedo.

For the class]80°, 90°] i.e., when the sun is close to the horizon, the cloud of points is larger. This is the effect of multiple interactions i.e., reflection and scattering, between sun rays and air molecules/clouds/ground surface along the long optical paths of sun rays in the atmosphere. In this case, the maximum value of PAR and broadband irradiances is less than 3 W m^{-2} and 7 W m^{-2} for ice and water clouds respectively, close to usual measurement uncertainties. Since these irradiances are quite low and insignificant in several applications and considering uncertainties affecting models and measurements at very large θ_s, all further analyses are limited to $\theta_s \leq 80°$.

Scatterplots similar to Fig. 3 were made for each value of τ_{cloud} as reported in Table 2. Similar observations were found as previously with very high r-squared correlation coefficient and clear linear relationship between $K^{BB}_{c\_RTS}$ and $K^{PAR}_{c\_RTS}$. Visual inspection reveals that the slope of the linear relationship increases with in-

Table 6: Fitting parameters a_1, a_2, a_3 for K_c^{PAR} retrievals for both cloud phases. Standard deviation is provided and attached to each value.

	Ice clouds	Water clouds
a_1	$8.734\times10^{-3}\pm9.816\times10^{-6}$	$7.175\times10^{-3}\pm2.432\times10^{-6}$
a_2	$-1.297\times10^{-4}\pm8.878\times10^{-8}$	$-9.191\times10^{-5}\pm2.488\times10^{-8}$
a_3	$6.914\times10^{-7}\pm1.187\times10^{-9}$	$4.509\times10^{-7}\pm7.028\times10^{-11}$

Table 7: Statistical indicators of the performances of the developed relationship for estimating K_c^{PAR} for numerical validations.

	Ice clouds	Water clouds
Number of data	567000	1260000
Mean	0.44	0.54
Bias (rbias)	−0.00 (−0.50 %)	−0.00 (−0.47 %)
STD (rSTD)	0.01 (2.15 %)	0.01 (1.97 %)
RMSE (rRMSE)	0.01 (2.21 %)	0.01 (2.03 %)
R^2	1.00	1.00

creasing τ_{cloud}. Therefore, K_c^{PAR} can be mathematically estimated as follows:

$$K_c^{\mathrm{PAR}} = AK_c^{\mathrm{BB}} \tag{5.1}$$

where the slope $A = f(\tau_{\mathrm{cloud}})$ is to be explicitly determined. One notes that in fully cloudy conditions meaning K_c^{BB} converging to zero, K_c^{PAR} converges to zero as expected.

Fig. 4 shows the slope A (on vertical axis) as a function of τ_{cloud} (on horizontal axis) for both cloud phases. Indeed, A depends strongly on τ_{cloud} and shows a tendency to increase with increasing τ_{cloud}. A can be well represented by an exponential function of polynomial of third degree. Therefore, Eq. (5.1) can be accurately approximated by:

$$K_c^{\mathrm{PAR}} = e^{a_1\tau_{\mathrm{cloud}}+a_2\tau_{\mathrm{cloud}}^2+a_3\tau_{\mathrm{cloud}}^3}K_c^{\mathrm{BB}} \tag{5.2}$$

where a_1, a_2, a_3 are parameters depending on the cloud phase obtained by least–square fitting and given in Table 6. Eq. (5.2) satisfies a constraint that in a fully clear-sky conditions where $K_c^{\mathrm{BB}} = 1$ meaning $\tau_{\mathrm{cloud}} = 0$, K_c^{PAR} is also equal to 1.

As for the direct component, we firstly performed a kind of validation by using as reference another set of libRadtran simulations (K_c^{BB}, K_c^{PAR}) built randomly following the distribution of variables described in Tables 1 and 2. The accuracy of the proposed relationship Eq. (5.2) was evaluated by comparing its outcomes to this new set of simulated K_c^{PAR}. Table 7 reports the statistical indicators for both cloud phases. Whatever the cloud phase, R^2 is 1.00. The bias is almost zero, i.e., less than −0.5 % in relative value. The RMSE is also almost zero, i.e., about 2 %. in relative value. These indicators prove the very good level of fitting for the developed relationships.

Then, we performed a comparison between the outcomes of Eq. (5.2) with "*RadFlux*" $K_{\mathrm{c\_meas}}^{\mathrm{BB}}$ and τ_{cloud} as inputs and the measured "*RadFlux*" $K_{\mathrm{c\_meas}}^{\mathrm{PAR}}$. Fig. 5 displays the 2D histogram between measured and estimated K_c^{PAR} including all stations. For both cloud phases, the points are elongated over the 1:1 line. Table 8 gives the statistical indicators. Estimated and measured K_c^{PAR} are very well correlated with R^2 greater than 0.98. The relative bias and relative RMSE are less than 3 % and reach up to 6 % respectively with a better performance for ice cloud phase.

Table 8: Statistical indicators of the performances of the developed relationship for estimating K_c^{PAR} using "*RadFlux*" data sets.

	Ice clouds	Water clouds
Nunber of data	406557	2055771
Mean	0.56	0.34
Bias (rbias)	−0.00 (−0.01 %)	0.01 (2.65 %)
STD (rSTD)	0.02 (4.40 %)	0.02 (5.96 %)
RMSE (rRMSE)	0.02 (4.40 %)	0.02 (6.53 %)
R^2	0.98	0.99

Table 9: Slopes of linear functions for inferring K_c^{PAR} from K_c^{BB}. Standard deviation is provided and associated to each value.

	Ice clouds	Water clouds
$0 < K_c^{\mathrm{BB}} < 1$	1.056 ± 0.000	1.059 ± 0.000
$K_c^{\mathrm{BB}} > 1$	1.017 ± 0.000	1.010 ± 0.000

5.2.2 For cases when uncertainty on COD is too large making COD useless

Taking into account the large uncertainties in estimates of τ_{cloud} (Turner et al., 2007) and more generally in cases when estimates of τ_{cloud} are unavailable, linear functions between K_c^{PAR} and K_c^{BB} were developed and found with RTS as follows:

$$K_c^{\mathrm{PAR}} = aK_c^{\mathrm{BB}} \tag{5.3}$$

with the slope a given in Table 9.

Eq. (5.3) was evaluated numerically and experimentally as carried out previously. Table 10 reports the statistical indicators summarizing the errors for both numerical and experimental validations. It has been found that Eq. (5.2) provides slightly better performance than Eq. (5.3).

5.2.3 For cases when no information on clouds is available

In the cases where both cloud phases are unavailable, the following relationships were found:

$$K_c^{\mathrm{PAR}} = bK_c^{\mathrm{BB}} \tag{5.4}$$

with $b = 1.058 \pm 0.000$ for $K_c^{\mathrm{BB}} \leq 1$, and $b = 1.011 \pm 0.000$ for $K_c^{\mathrm{BB}} > 1$

Eq. (5.4) was evaluated numerically and experimentally as carried out previously. Table 11 reports the statistical indicators summarizing the errors for both numer-

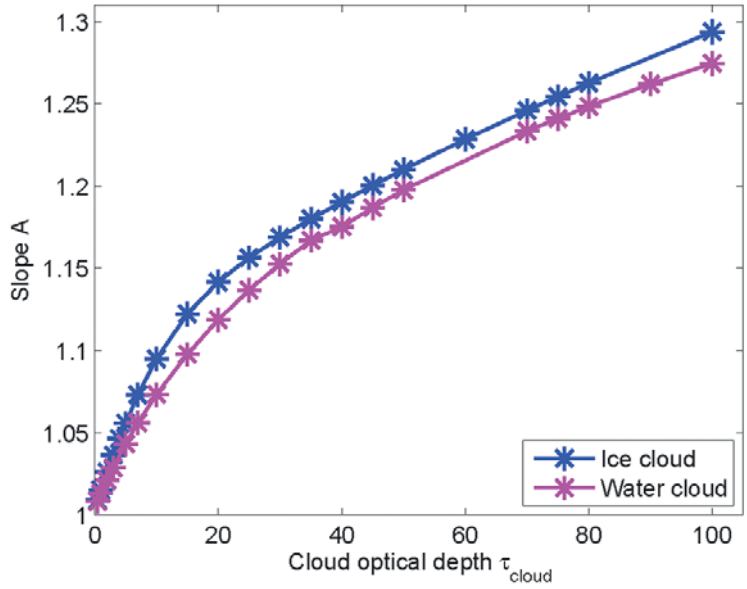

Figure 4: Relationship between the slope A (on vertical axis) and the cloud optical depth τ_{cloud} for both cloud phases.

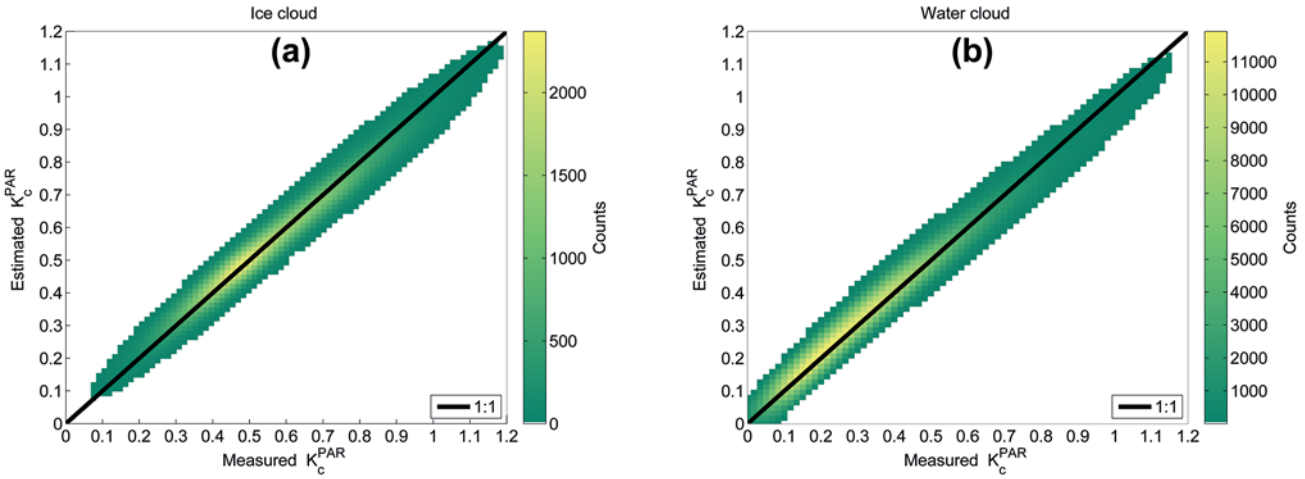

Figure 5: 2D histogram of measured (horizontal axis) and estimated (vertical axis) K_c^{PAR}. (a) for ice clouds and (b) for water clouds. The color bar indicates the number of pairs in each class.

ical and experimental validations. In order to compare with the previous relationships, results are presented for ice and water clouds. One may observe that the correlation is very high with R^2 equal to 0.99. The other statistical indicators are slightly (a bit greater, significantly) greater than those of the other relationships.

6 In practice

Fig. 6 summarises how to exploit all developed relationships for estimating K_c^{PAR} from K_c^{BB} considering the availability or not of τ_{cloud} and cloud phase. At the best when all inputs are available, for instance, CAMS-Rad model can be used to retrieve all necessary cloud properties from the combination APOLLO (AVHRR Processing scheme Over cLouds, Land and Ocean; Kriebel et al., 1989; 2003) scheme and SEVIRI (Spinning Enhanced Visible and Infrared Imager) instrument such as COD, cloud type including four categories: low, medium, high for water clouds and thin for ice clouds, and cloud coverage similar to broadband fractional sky cover (mask) for the pixel under concern. Overall, the PAR fluxes under cloudy conditions can be retrieved by using the clear-sky PAR fluxes from Wandji Nyamsi et al. (2019) and then multiply by the PAR clear-sky index retrieved from appropriate equations of the developed relationships following Fig. 6.

7 Conclusion

Empirical relationships between PAR and broadband clear-sky indices have been developed and assessed here. A great benefit of these relationships is that they take advantage of the large availability of broadband clear-sky indices from measurements, satellite-based retrievals or meteorological reanalyses. In the view of the

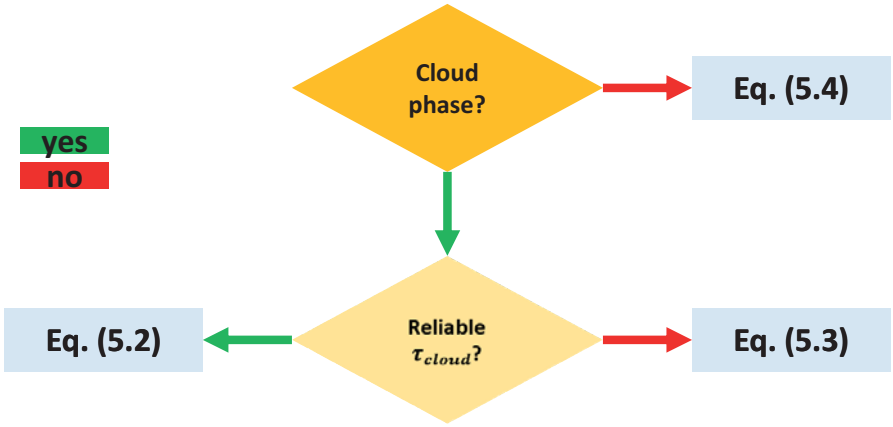

Figure 6: Sketch of algorithm to convert K_c^{BB} into K_c^{PAR} taking into account the availability of cloud phase and τ_{cloud}.

Table 10: Statistical indicators of Eq. (5.3) for both numerical and experimental validations. Experimental validations are in bold.

	Ice cloud	Water cloud
Number of data	567000 / **406557**	1260000 / **2055771**
Mean	0.44 / **0.56**	0.54 / **0.34**
Bias (rbias)	−0.01 (−2.62 %) / **0.01 (1.19 %)**	−0.01 (−2.23 %) / **−0.01 (−1.81 %)**
STD (rSTD)	0.03 (5.88 %) / **0.02 (4.28 %)**	0.03 (5.76 %) / **0.02 (6.52 %)**
RMSE (rRMSE)	0.03 (6.44 %) / **0.02 (4.44 %)**	0.03 (6.18 %) / **0.02 (6.76 %)**
R^2	0.99 / **0.98**	0.99 / **0.99**

Table 11: Statistical indicators of Eq. (5.4) for both numerical and experimental validations. Experimental validations are in bold.

Number of data	1827000 / **2462315**
Mean	0.51 / **0.37**
Bias (rbias)	−0.01 (−2.36 %) / **−0.00 (−1.08 %)**
STD (rSTD)	0.03 (5.80 %) / **0.02 (6.13 %)**
RMSE (rRMSE)	0.03 (6.26 %) / **0.02(6.22 %)**
R^2	0.99 / **0.99**

authors, it is a complementary step accounting for cloud attenuation of PAR irradiances yielding to all-sky PAR estimates following the assumption that all-sky PAR flux can be accurately expressed as the product of clear-sky PAR flux and PAR clear-sky index as suggested by Bosch et al. (2009), Oumbe et al. (2014) or Wandji Nyamsi et al. (2019).

Overall, the relationships found between broadband, and PAR clear-sky indices are linear. For instance, the slope of the function can be set to a constant if the cloud optical phase (COD) is unknown/unreliable or is an exponential function of polynomial of the COD without a noticeable loss of accuracy. The estimates from the developed relationships were assessed (1) numerically by using detailed spectral calculations of the radiative transfer model and (2) against their counterparts obtained from ground-based measurements serving as reference. Taking the cloud phase into account or not, the correlation coefficient is greater than 0.98. The relative bias in absolute value and the root mean square error are less than 3 % and 6 % respectively denoting a high level of performance. We found that the performance is slightly better when using accurate COD when available.

The present study has a practical implication as it provides useful relationships easy to implement for deriving PAR clear-sky index from broadband clear-sky index. In practise and for operational purposes, linear functions are a very good compromise for estimating PAR clear-index. This opens the way for accurate estimates of all-sky PAR irradiances. There is no evidence known to the authors that the proposed relationships may not work properly at any site in the world under any sky conditions. Nevertheless, this should be proven by further validation in various climatic conditions where PAR measurements are available.

Author Contributions

WWN and LW conceived and designed the presented study. WWN, YMSD, JAA, AA and LW designed the methodology. JAA identified the relevant sources of measurements from stations and WWN collected the measurements. WWN performed radiative transfer simulations and all necessary computations. All authors participated in investigating and interpreting the results. WWN wrote the original manuscript and all authors participated in writing and editing the manuscript.

Funding

The research leading to these results has received partial funding from the Framework Partnership Agreement on Copernicus User Uptake of the European Union

through the French Spatial Agency CNES. The paper is supported by the European Union's Caroline Herschel Framework Partnership Agreement on Copernicus User Uptake under grant agreement No FPA 275/G/GRO/COPE/17/10042, project FPCUP (Framework Partnership Agreement on Copernicus User Uptake), Action No, Action title, SGA#12.

Data availability statement

All measurements at each station were provided by the SURFRAD network established in 1993 through the support of the NOAA Office of Global Programs. Measurements used here are freely available and were downloaded from https://gml.noaa.gov/aftp/data/radiation/surfrad/ and https://gml.noaa.gov/aftp/data/radiation/surfrad/RadFlux/, accessed on 2022-10-01. The simulated data presented in this paper were created by radiative transfer model simulations. They are freely available through direct contact with the corresponding author.

Acknowledgments

The authors thank the teams developing libRadtran (http://www.libradtran.org, accessed on 2023-02-01) and the NOAA ESRL Global Monitoring Division, Boulder, Colorado, USA (http://esrl.noaa.gov/gmd/, accessed on 2022-10-01) for offering free access to SURFRAD data. WWN thanks Claire Thomas for interesting discussions and feedback.

References

Akitsu, T., A. Kume, Y. Hirose, O. Ijima, K.N. Nasahara, 2015: On the stability of radiometric ratios of photosynthetically active radiation to global solar radiation in Tsukuba, Japan. – Agric. For. Meteorol. **209**, 59–68. DOI:10.1016/j.agrformet.2015.04.026.

Augustine, J.A., J.J. Deluisi, C.N. Long, 2000: SURFRAD – A national surface radiation budget network for atmospheric research. – Bull. Amer. Meteor. Soc. **81**, 2341–2357. DOI:10.1175/1520-0477(2000)081<2341:SANSRB>2.3.CO;2.

Barnard, J.C., C.N. Long, E.I. Kassianov, S.A. Mcfarlane, J.M. Comstock, M. Freer, G.M. Mcfarquhar, 2008: Development and evaluation of a simple algorithm to find cloud optical depth with emphasis on thin ice clouds. – Open Atmos. Sci. J. **2**, 46–55. DOI:10.2174/1874282300802010046.

Bosch, J.L., G. López, F.J. Batlles, 2009: Global and direct photosynthetically active radiation parameterizations for clear-sky conditions. – Agric. For. Meteorol. **149**, 146–158. DOI:10.1016/j.agrformet.2008.07.011.

Calbó, J., D. Pages, J.A. González, 2005: Empirical studies of cloud effects on UV radiation: A review. – Rev. Geophys. **43**, RG2002. DOI:10.1029/2004RG000155.

Den Outer, P.N., H. Slaper, J. Kaurola, A. Lindfors, A. Kazantzidis, A.F. Bais, U. Feister, J. Junk, M. Janouch, W. Josefsson, 2010: Reconstructing of erythemal ultraviolet radiation levels in Europe for the past 4 decades. – J. Geophys. Res. Atmos. **115**, D10102. DOI:10.1029/2009JD012827.

Emde, C., R. Buras-Schnell, A. Kylling, B. Mayer, J. Gasteiger, U. Hamann, J. Kylling, B. Richter, C. Pause, T. Dowling, L. Bugliaro, 2016: The libRadtran software package for radiative transfer calculations (version 2.0.1). – Geosci. Model Dev. **9**, 1647–1672. DOI:10.5194/gmd-9-1647-2016.

Escobedo, J.F., E.N. Gomes, A.P. Oliveira, J. Soares, 2009: Modeling hourly and daily fractions of UV, PAR and NIR to global solar radiation under various sky conditions at Botucatu, Brazil. – Appl. Energy **86**, 299–309. DOI:10.1016/J.Apenergy.2008.04.013.

Frolking, S.E., J.L. Bubier, N.T. Roulet, A.E. Suyker, S.B. Verma, J.M. Waddington, G.J. Whiting, T.R. Moore, T. Ball, L.M. Bellisario, A. Bhardwaj, P. Carroll, P.M. Crill, P.M. Lafleur, J.H. Mccaughey, 1998: Relationship between ecosystem productivity and photosynthetically active radiation for northern peatlands. – Global Biogeochem. Cycles **12**, 115–126. DOI:10.1029/97GB03367.

Frouin, R., H. Murakami, 2007: Estimating photosynthetically available radiation at the ocean surface from ADEOS-II global imager data. – J. Oceanogr. **63**, 493–503. DOI:10.1007/s10872-007-0044-3.

Fu, Q.,1996: An accurate parameterization of the solar radiative properties of cirrus clouds for climate models. – J. Climate **9**, 2058–2082. DOI:10.1175/1520-0442(1996)009<2058:AAPOTS>2.0.CO;2.

Gonzalez, J.A., J. Calbo, 2002: Modelled and measured ratio of PAR to global radiation under cloudless skies. – Agric. For. Meteorol. **110**, 319–325. DOI:10.1016/S0168-1923(01)00291-X.

Gueymard, C.A., 2004: The sun's total and the spectral irradiance for solar energy applications and solar radiations models. – Sol. Energy **76**, 423–452, DOI:10.1016/j.solener.2003.08.039.

Gschwind, B., L. Ménard, M. Albuisson, L. Wald, 2006: Converting a successful research project into a sustainable service: The case of the SoDa Web service. – Env. Model. Softw. **21**, 1555–1561. DOI:10.1016/j.envsoft.2006.05.002.

Gschwind, B., L. Wald, P. Blanc, M. Lefevre, M. Schroedter-Homscheidt, A. Arola, 2019: Improving the McClear model estimating the downwelling solar radiation at ground level in cloud-free conditions – McClear-v3. – Meteorol. Z. **28**, 147–163. DOI:10.1127/metz/2019/0946.

Hess, M., P. Koepke, I. Schult, 1998: Optical properties of aerosols and clouds: The software package OPAC. – Bull. Amer. Meteor. Soc. **79**, 831–844. DOI:10.1175/1520-0477(1998)079<0831:OPOAAC>2.0.CO;2.

Hu, Y.X., K. Stamnes, 1993: An accurate parameterization of the radiative properties of water clouds suitable for use in climate models. – J. Climate **6**, 728–742. DOI:10.1175/1520-0442(1993)006<0728:AAPOTR>2.0.CO;2.

Huang, G.H., M.G. Ma, S.L. Liang, S.M. Liu, X. Li, 2011: A LUT-based approach to estimate surface solar irradiance by combining MODIS and MTSAT data. – J. Geophys. Res. Atmos. **116**, D22201. DOI:10.1029/2011JD016120.

ISO, 1995: Guide to the Expression of Uncertainty in Measurement: first edition. – International Organization for Standardization, Geneva, Switzerland.

Jacovides, C.P., F.S. Timvios, G. Papaioannou, D.N. Asimakopoulos, C.M. Theofilou, 2004: Ratio of PAR to broadband solar radiation measured in Cyprus. – Agric. For. Meteorol. **121**, 135–140. DOI:10.1016/j.agrformet.2003.10.001.

Jacovides, C.P., F.S. Tymvios, J. Boland, M. Tsitouri, 2015: Artificial neural network models for estimating daily solar global UV, PAR and broadband radiant fluxes in an east-

ern Mediterranean site. – Atmos. Res., **152**, 138–145. DOI: 10.1016/j.atmosres.2013.11.004.

Kriebel, K.T., R.W. Saunders, G. Gesell, 1989: Optical properties of clouds derived from fully cloudy AVHRR pixels. – Beiträge zur Physik der Atmosphäre **62**, 165–171.

Kriebel, K.T., G. Gesell, M. Kastner, H. Mannstein, 2003: The cloud analysis tool APOLLO: improvements and validations. – Int. J. Remote Sens. **24**, 2389–2408. DOI:10.1080/01431160210163065.

Krotkov, N.A., J.R. Herman, P.K. Bhartia, V. Fioletov, Z. Ahmad, 2001: Satellite estimation of spectral surface UV irradiance: 2. Effects of homogeneous clouds and snow. – J. Geophys. Res. Atmos. **106**, 11743–11759. DOI:10.1029/2000JD900721.

Lefèvre, M., A. Oumbe, P. Blanc, B. Espinar, B. Gschwind, Z. Qu, L. Wald, M. Schroedter-Homscheidt, C. Hoyer-Klick, A. Arola, A. Benedetti, J.W. Kaiser, J.-J. Morcrette, 2013: McClear: a new model estimating downwelling solar radiation at ground level in clear-sky conditions. – Atmos. Meas. Tech. **6**, 2403–2418. DOI:10.5194/amt-6-2403-2013.

Li, T., Q. Yang, 2015: Advantages of diffuse light for horticultural production and perspectives for further research. – Front. Plant Sci. **6**, 704. DOI:10.3389/fpls.2015.00704.

Long, C.N., 2005: On the estimation of clear-sky upwelling SW and LW. – 15th ARM Science Team Meeting Proceedings, Daytona Beach, Florida, March 14–18.

Long, C.N., T.P. Ackerman, 2000: Identification of clear skies from broadband pyranometer measurements and calculation of downwelling shortwave cloud effects. – J. Geophys. Res. Atmos. **105**, D12, 15609–15626. DOI:10.1029/2000JD900077.

Long, C.N., K.L. Gaustad, 2004: The Shortwave (SW) Clear-Sky Detection and Fitting Algorithm: Algorithm Operational Details and Explanations, Atmospheric Radiation Measurement Program Technical Report, ARM TR-004. – Available at http://www.arm.gov (accessed 1.11.2022).

Long, C.N., T.P. Ackerman, K.L. Gaustad, J.N.S. Cole, 2006: Estimation of fractional sky cover from broadband shortwave radiometer measurements. – J. Geophys Res. **111**, D11204. DOI:10.1029/2005JD006475.

Mayer, B., A. Kylling, 2005: The libRadtran software package for radiative transfer calculations-description and examples of use. – Atmos. Chem. Phys. **5**, 1855–1877. DOI:10.5194/acp-5-1855-2005.

Mccree, K.J., 1972: Test of current definitions of photosynthetically active radiation against leaf photosynthesis data. – Agr. Forest. Meteorol. **10**, 443–453. DOI:10.1016/0002-1571(72)90045-3.

Mccree, K.J., 1981: Photosynthetically active radiation. – In: Physiological plant ecology I. Springer, Berlin, Heidelberg, 41–55.

Mottus, M., J. Ross, M. Sulev, 2001: Experimental study of ratio of PAR to direct integral solar radiation under cloudless conditions. – Agric. For. Meteorol. **109**, 161–170. DOI: 10.1016/S0168-1923(01)00269-6.

Mueller, R., T. Behrendt, A. Hammer, A.A. Kemper, 2012: New algorithm for the satellite-based retrieval of solar surface irradiance in spectral bands. – Remote Sens. **4**, 622–647, DOI: 10.3390/rs4030622.

Oumbe, A., Z. Qu, P. Blanc, M. Lefèvre, L. Wald, S. Cros, 2014: Decoupling the effects of clear atmosphere and clouds to simplify calculations of the broadband solar irradiance at ground level. – Geosci. Model Dev. *7*, 1661–1669, Corrigendum **7**, 2409–2409, DOI:10.5194/gmd-7-1661-2014.

Piedehierro, A.A., M. Antón, A. Cazorla, L. Alados-Arboledas, F.J. Olmo, 2014: Evaluation of enhancement events of total solar irradiance during cloudy conditions at Granada (Southeastern Spain). – Atmos. Res. **135**, 1–7. DOI: 10.1016/j.atmosres.2013.08.008.

Qu, Z., A. Oumbe, P. Blanc, B. Espinar, G. Gesell, B. Gschwind, L. Klüser, M. Lefèvre, L. Saboret, M. Schroedter-Homscheidt, L. Wald, 2017: Fast radiative transfer parameterisation for assessing the surface solar irradiance: The Heliosat-4 method. – Meteorol. Z. **26**, 33–57. DOI: 10.1127/metz/2016/0781.

Sabburg, J., J. Calbó, 2009: Five years of cloud enhanced surface UV radiation measurements at two sites (in the Northern and Southern Hemispheres). – Atmos. Res. **93**, 902–912. DOI: 10.1016/j.atmosres.2009.05.003.

Stamnes, K., S.-C. Tsay, W. Wiscombe, K. Jayaweera, 1988. Numerically stable algorithm for discrete-ordinate-method radiative transfer in multiple scattering and emitting layered media. – Appl. Opt. **27**, 2502–2509. DOI:10.1364/AO.27.002502.

Stamnes, K., S.-C. Tsay, W. Wiscombe, I. Laszlo, 2000: DISORT, a general-purpose Fortran program for discrete ordinate method radiative transfer in scattering and emitting layered media: Documentation of methodology. – Tech. Rep., Dept. of Physics and Engineering Physics, Stevens Institute of Technology, Hoboken, NJ07030, USA.

Thomas, C., S. Dorling, W. Nyamsi, L. Wald, S. Rubino, L. Saboret, M. Trolliet, E. Wey, 2019: Assessment of five different methods for the estimation of surface photosynthetically active radiation from satellite imagery at three sites – application to the monitoring of indoor soft fruit crops in souther n UK. – Adv. Sci. Res. **16**, 229–240. DOI:10.5194/asr-16-229-2019.

Turner, D.D., A.M. Vogelmann, R.T. Austin, J.C. Barnard, K. Cady-Pereira, J.C. Chiu, S.A. Clough, C. Flynn, M.M. Khaiyer, J. Liljegren, K. Johnson, 2007: Thin liquid water clouds: Their importance and our challenge. – Bull. Amer. Meteor. Soc. **88**, 177–190. DOI:10.1175/BAMS-88-2-177.

Udo, S.O., T.O. Aro, 1999: Global PAR related to global solar radiation for central Nigeria. – Agric. For. Meteorol. **97**, 21–31. DOI:10.1016/S0168-1923(99)00055-6.

Vindel, J.M., R.X. Valenzuela, A.A. Navarro, L.F. Zarzalejo, A. Paz-Gallardo, J.A. Souto, R. Méndez-Gómez, D. Cartelle, J.J. Casares, 2018: Modeling photosynthetically active radiation from satellite-derived estimations over mainland Spain. – Remote Sens. **10**, 849. DOI:10.3390/rs10060849.

Wald, L., 2021: Fundamentals of Solar Radiation. – CRC Press, Boca Raton, 267 pp, DOI:10.1201/9781003155454.

Wandji Nyamsi, W., B. Espinar, P. Blanc, L. Wald, 2014: How close to detailed spectral calculations is the k-distribution method and correlated-k approximation of Kato et al. (1999) in each spectral interval? – Meteorol. Z. **23**, 547–556. DOI: 10.1127/metz/2014/0607.

Wandji Nyamsi, W., B. Espinar, P. Blanc, L. Wald, 2015a: Estimating the photosynthetically active radiation under clear skies by means of a new approach. – Adv. Sci. Res. **12**, 5–10. DOI:10.5194/asr-12-5-2015.

Wandji Nyamsi, W., A. Arola, P. Blanc, A.V. Lindfors, V. Cesnulyte, M.R.A. Pitkänen, L. Wald, 2015b: A novel parameterization of the transmissivity due to ozone absorption in the *k*-distribution method and correlated-k approximation of Kato et al. (1999) over the UV band. – Atmos. Chem. Phys. **15**, 7449–7456. DOI:10.5194/acp-15-7449-2015.

Wandji Nyamsi, W., M. Pitkänen, Y. Aoun, P. Blanc, A. Heikkilä, K. Lakkala, G. Bernhard, T. Koskela, A.V. Lindfors, A. Arola, L. Wald, 2017: A new method for estimating UV fluxes at ground level in cloud-free condi-

tions. – Atmos. Meas. Techn. **10**, 4965–4978. DOI:10.5194/amt-10-4965-2017.

Wandji Nyamsi, W., P. Blanc, J.A. Augustine, A. Arola, L. Wald, 2019: A new clear-sky method for assessing photosynthetically active radiation at the surface level. – Atmosphere **10**, 219. DOI:10.3390/atmos10040219.

Wandji Nyamsi, W., P. Blanc, D. Dumortier, R. Mouangue, A. Arola, L. Wald, 2021: Using Copernicus Atmosphere Monitoring Service (CAMS) products to assess illuminances at ground level under cloudless conditions. – Atmosphere **12**, 643. DOI:10.3390/atmos12050643.

Wandji Nyamsi, W., Y.-M. Saint-Drenan, A. Arola, L. Wald, 2023: Further validation of the estimates of the downwelling solar radiation at ground level in cloud-free conditions provided by the McClear service: the case of Sub-Saharan Africa and the Maldives Archipelago. – Atmos. Meas. Tech. **16**, 2001–2036. DOI:10.5194/amt-16-2001-2023.

Zhang, X., Y. Zhang, Y. Zhoub, 2000: Measuring and modelling photosynthetically active radiation in Tibet Plateau during April-October. – Agric. For. Meteorol. **102**, 207–212. DOI:10.1016/S0168-1923(00)00093-9.